



TECHNICAL ARTICLE

# Effects of Ti and Nb Additions on Microstructure and Shape Memory Effect of Fe-10Mn-6Si-4Ni-7Cr-0.3C Shape Memory Alloy

AQEEL ABBAS,<sup>1,3</sup> JUNG-WEI HSU,<sup>2</sup> SYED MURAWAT ABBAS NAQVI,<sup>3</sup>  
HSIN-CHIH LIN,<sup>1,4</sup> and KUN-MING LIN<sup>2,5</sup>

1.—Department of Materials Science and Engineering, National Taiwan University, Taipei 10617, Taiwan. 2.—Department of Materials Science and Engineering, Feng Chia University, Taichung 40724, Taiwan. 3.—Department of Mechanical Engineering, NFC-Institute of Engineering and Fertilizer Research Faisalabad, Faisalabad, Pakistan. 4.—e-mail: hclinntu@ntu.edu.tw. 5.—e-mail: kmlin@fcu.edu.tw

The iron-based shape memory alloys have found applications in the pharmaceutical and aerospace industries for their light weight and excellent shape memory effects. The shape memory effects and corrosion properties are significantly influenced by additives and heat treatments. Vacuum arc remelting was employed to prepare Fe-10Mn-6Si-4Ni-7Cr-0.3C-*m*Ti/*n*Nb (*m* = 0.1, 0.3, 0.5, 0.7, *n* = 0.05, 0.1, 0.3, 0.5) shape memory alloys. The samples were hot-rolled at 1100°C and solution heat-treated at 1150°C for 1 h. The shape memory effect, microstructure, and corrosion performance of Fe-10Mn-6Si-4Ni-7Cr-0.3C-*m*Ti/*n*Nb were analyzed at higher aging temperatures. The microstructural investigations indicate that large amounts of TiC, NbC, Cr<sub>23</sub>C<sub>6</sub>, and Cr<sub>7</sub>C<sub>3</sub> phases are precipitated when aged at 800°C, leading to improvement of the shape memory effect of the alloys. The shape recovery ratio reaches 89.9%, 89.5%, 91.1%, and 74.4% for the alloys with 0.1 Ti, 0.3 Ti, 0.5 Ti, and 0.7Ti additions, respectively, at 800°C aging temperature under 3% bending strain. The aging at 500°C increased the shape memory effect by 20–30%, while further aging at 700°C only improved it by a further 10–20%. The shape recovery ratio of alloys with 0.05 Nb and 0.1 Nb reached a maximum of 88.6% and 88.4%, respectively, when aged at 900°C, while, when aged at 800°C, 0.3 Nb and 0.5 Nb reached 83.7%, and 82.9%, respectively. The shape recovery ratio of the alloys with Nb was increased by about 5–30% compared to that with no Nb. The addition of Ti/*n*Nb and aging at higher temperatures improved the corrosion resistance in 3.5-wt.% NaCl solution owing to the formation of Ti/Nb carbide more easily than Cr carbide, leaving a higher content of Cr in the matrix of the alloys.

## INTRODUCTION

Significant importance is given to functional and structural materials with development in science and technology.<sup>1,2</sup> Shape memory alloys (SMAs) are considered as functional materials for shape recovery applications.<sup>3,4</sup> The most commonly used SMAs are Ni-Ti-based, Fe-based, and Cu-based for their

better corrosion resistance, good plasticity, and relatively low cost.<sup>5,6</sup> Fe-based shape memory alloys are relatively less expensive and have higher strength.<sup>7</sup> There are several iron-based SMAs, including FeNiCoTi, FeNiC, FePd, FePt, and FeMnSi.<sup>8</sup> FeMnSi-based SMAs are improved from the FeMn alloy, and the shape memory mechanism is mainly produced by the mutual conversion of  $\gamma$  austenite and  $\varepsilon$  martensite.<sup>9</sup> If both  $\varepsilon$  martensite and  $\alpha'$  martensite exist in the alloy,  $\alpha'$  martensite

will hinder the reverse phase transformation of  $\varepsilon$  martensite  $\rightarrow \gamma$  austenite and the shape memory effect is reduced.<sup>10</sup>

The shape memory effect of the SMAs can be controlled by changing the composition to meet the requirement of the application. FeMnSi-based SMAs are being developed, and the Ms temperature can be reduced to room temperature by additives and heat treatments while maintaining the excellent shape memory effect.<sup>11</sup> The Ms and Af temperatures of the SMAs increase with the increase in the number of cycles, and the shape memory effect will be greatly reduced.<sup>12</sup> Rare-earth elements (Ti, V, Nb, and Mn) are added to improve the thermal stability of Fe-SMAs.<sup>13–15</sup> Although the addition of rare-earth elements improves the thermal stability, Fe-based SMAs still have shortcomings, such as grain boundary brittleness and the poor fatigue characteristics of polycrystalline alloys, resulting in limited applications.<sup>3,16–18</sup>

FeMnSi-based SMAs have been developed with the best composition of Fe-10Mn-6Si-4Ni-7Cr-0.3C and aged heat-treated at the different higher temperatures. Fe-10Mn-6Si-4Ni-7Cr-0.3C presented the excellent shape recovery ratio of 85% at 800°C. The shape recovery ratio of the Fe-10Mn-6Si-4Ni-7Cr-0.3C alloy can be further improved by adding rare-earth metals such Ti and Nb to increase their Ms temperature and Neel temperature ( $T_n$ ).<sup>19,20</sup> The  $T_n$  temperature indicates the magnetism and is defined as the transition temperature from paramagnetic to diamagnetism. The diamagnetism is more likely to produce an ordered structure to stabilize the matrix structure, making the alloy less easy to transform.<sup>21,22</sup> The addition of Cr, Ti, Nb, and Ni to the alloy can also reduce the  $T_n$  temperature, strengthen the  $\gamma$  parent phase, and reduce the stress required to induce  $\varepsilon$  martensite.<sup>23</sup> The heat treatment and severe plastic deformation improve the shape memory effect by grain refinement and  $\varepsilon$  martensite repositioning.<sup>24</sup> The nucleation position of  $\varepsilon$  martensite can be increased to enhance the amount of phase transformation of  $\gamma \rightarrow \varepsilon$  to obtain the shape.<sup>14</sup>

FeMnSi-based SMAs were investigated, and Fe-10Mn-6Si-4Ni-7Cr-0.3C was observed to be the best alloy, having an excellent shape memory effect at 800°C aging temperature. Fe-10Mn-6Si-4Ni-7Cr-0.3C alloys with different Ti and Nb compositions were manufactured using vacuum arc melting (VAR) followed by hot rolling and higher temperature aging. The microstructure and shape memory effect of the SMAs were investigated at the higher temperature. The corrosion resistance performance of the alloy with the best shape memory effect was analyzed.

## EXPERIMENTAL PROCEDURES AND METHODS

Fe-10Mn-6Si-4Ni-7Cr-0.3C SMAs with different concentrations of titanium (Ti) and niobium (Nb) were prepared using the VAR process. The (SMAs

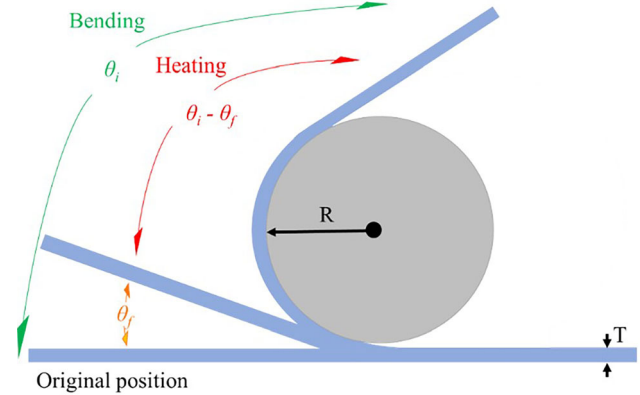


Fig. 1. Schematic of the bending test.

were subsequently hot-rolled at a rolling speed of 0.7 m/min at 1100°C, with a thickness reduction of 0.5 mm after each pass. The hot-rolled samples were homogenized at 1150°C for 1 h, followed by water quenching. The quenched samples were then aged for 1 h at 500–900°C and quenched in water. Standard metallographic techniques were employed to prepared specimens for microstructural observations. The polished samples were etched in 20% Nital solution. A variable vacuum scanning electron microscope (Hitachi S3400N) equipped with energy dispersive spectrometer (EDS) was employed for microstructural analysis. An X-ray diffractometer (XRD; Bruker D2) using the characteristic wavelength  $\lambda = 1.542 \text{ \AA}$ , scanning rate of  $1.2^\circ/\text{min}$  and diffraction angle of  $2\theta$  ranging from  $20^\circ$  to  $80^\circ$  was employed to analyze the phase composition. The operating voltage of D2 phaser was set to 30 kV and the operating current was 10 mA.

An electronic probe microanalyzer (EPMA; JEOL JXA-8200) was used to observe the distribution of elements in the alloy and to infer the composition of the second-phase precipitates. A double-jet electropolishing machine (EAFischione-120) using the corrosive liquid, 10% perchloric acid, at the operating temperature of  $-30^\circ\text{C}$  to  $-40^\circ\text{C}$  was employed for electropolishing prior to transmission electron microscopy (TEM; Tecnai G2) analysis to observe and analyze the structure and composition of the material. Bright-field, darkfield, and selection area electron diffraction (SADP) images were obtained for analysis.

The shape memory effect of the SMAs was analyzed using bending tests by measuring the shape recovery ratio at different temperatures. Strip specimens with dimensions of  $2.0 \text{ mm} \times 2.0 \text{ mm} \times 60 \text{ mm}$  were used in the bending tests. A schematic of the bending test is shown in Fig. 1. The specimens were bent to the appropriate angle of  $\theta_i$  using a special mold and then heated in a high-temperature furnace to  $A_f$  ( $600^\circ\text{C}$ ) for 10 min. The specimen returned to another angle,  $\theta_f$ . The shape recovery rate of the SMAs was determined using:

Effects of Ti and Nb Additions on Microstructure and Shape Memory  
 Effect of Fe-10Mn-6Si-4Ni-7Cr-0.3C Shape Memory Alloy

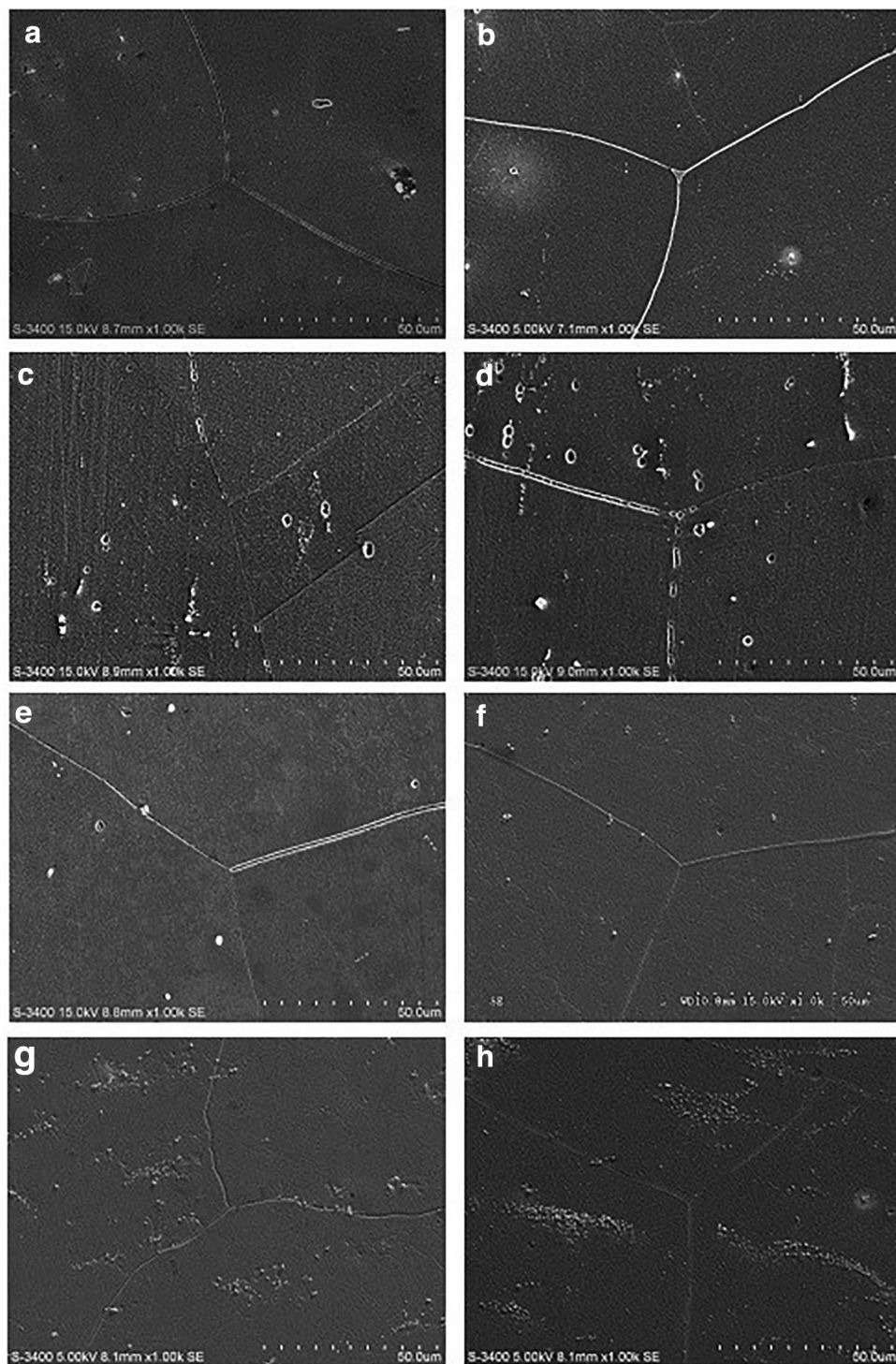


Fig. 2. SEM images of each alloy after solution treatment: (a) 10Mn7Cr 0.1Ti, (b) 10Mn7Cr 0.3Ti, (c) 10Mn7Cr 0.5Ti, (d) 10Mn7Cr 0.7Ti, (e) 10Mn7Cr 0.05Nb, (f) 10Mn7Cr 0.1Nb, (g) 10Mn7Cr 0.3Nb, and (h) 10Mn7Cr 0.5Nb.

$$RSME (\%) = (\theta_i - \theta_f) / \theta_i \times 100 \quad (1)$$

The electrochemical corrosion was carried out using a standard three-electrode potentiostat in 3.5-wt.% NaCl solution. Saturated calomel was used as the reference electrode, platinum as the counter

electrode, and the sample as the working electrode. The potentiodynamic current-potential curves (Tafel curves) were recorded from -2 V to +2 V at the scan rate of 5 mV/min. The open-circuit potential was recorded after immersion of the electrode in the solution for 1 h (versus Ag/AgCl). The corrosion

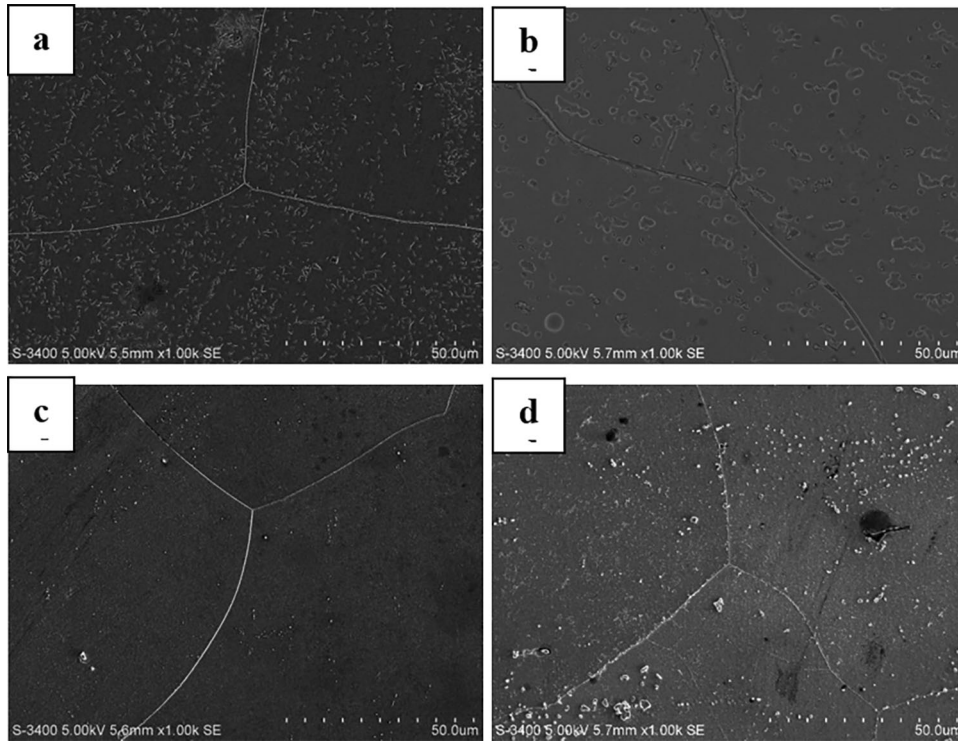


Fig. 3. SEM images of: (a) 10Mn7Cr 0.1Ti, (b) 10Mn7Cr 0.3Ti, (c) 10Mn7Cr 0.5Ti, and (d) 10Mn7Cr 0.7Ti alloys after aging at 800°C.

current density and corrosion potential were measured on the potentiodynamic curves using the tangent line method.

## RESULTS AND DISCUSSION

### Microstructural Observations

The SEM images of Fe-10Mn-6Si-4Ni-7Cr-0.3C-mTi/nNb alloys after solution treatment are presented in Fig. 2. It can be observed that second-phase precipitates appear in the alloy with Ti and Nb. It is inferred that the precipitates are formed at higher temperatures and had not been dissolved. The parent  $\gamma$  austenite (FCC) phase and  $\epsilon$  martensite (HCP) phase coexist after solid-solution treatment. The results are also consistent with the XRD data in which  $\epsilon$  martensite signal peaks appear in all the samples. The addition of Cr lowers the Ms temperature and strengthens the parent  $\gamma$  austenite phase. The higher peak intensity in the XRD diffraction pattern endorses that the Cr addition strengthens the  $\gamma$  austenite phase.

Figure 3 presents the SEM images of Fe-10Mn-6Si-4Ni-7Cr-0.3C-xTi alloys aged at 800°C. A large number of precipitates are formed, which leads to enhancement in the shape memory effects. The addition of Ti in Fe-10Mn-6Si-4Ni-7Cr-0.3C alloys has formed TiC phases after aging at 800°C. The TiC precipitates are irregular granular and the Cr carbides are rod-like-shaped at lower aging temperatures. The higher aging temperature indicates that all the carbides (Ti carbides and Cr carbides) appear

in granular shapes and coexist. Larger proportions of Cr carbides appeared, leading to the enhancement of the shape memory effects.<sup>9,17</sup> The best composition alloy, 10Mn7Cr0.5Ti, was selected for EPMA analysis (Fig. 4) to investigate the distribution of particles at 800°C. It can be found from Fig. 4 that two kinds of carbides have been observed at the 800°C aging temperature. A large amount of  $\text{Cr}_{23}\text{C}_6$  is precipitated on the grain boundary and  $\text{Cr}_7\text{C}_3$  in the base. The TiC is also present because the melting point of TiC is higher than the solution treatment temperature and cannot form a residue in the alloy. The shape of  $\text{Cr}_7\text{C}_3$  tends to be rod-like and elongated, while the shape of TiC is irregular granular.

Figure 5 presents the SEM images of Fe-10Mn-6Si-4Ni-7Cr-0.3C-nNb alloys after 800°C aging heat treatment. It can be seen that a large amount of chromium carbide and a small amount of NbC are precipitated. The second phase of Cr carbides is  $\text{Cr}_{23}\text{C}_6$ , and  $\text{Cr}_7\text{C}_3$  is also precipitated. It can also be seen in Fig. 5 that  $\text{Cr}_{23}\text{C}_6$  and  $\text{Cr}_7\text{C}_3$  are rod-shaped, and that NbC is irregular granular. The precipitation of Cr is also significantly reduced after aging at 800°C with the addition of 0.3 Nb and 0.5 Nb. The Cr carbides are significantly decreased with the increase of Nb contents.<sup>25</sup> The excess addition of Nb and higher-temperature aging will inhibit the formation of  $\text{Cr}_{23}\text{C}_6$  and  $\text{Cr}_7\text{C}_3$ . The EPMA analysis of the 10Mn7Cr0.05Nb alloy after 800°C aging treatment is presented in Fig. 6. Both Nb and Cr carbides are formed. The Cr carbides are

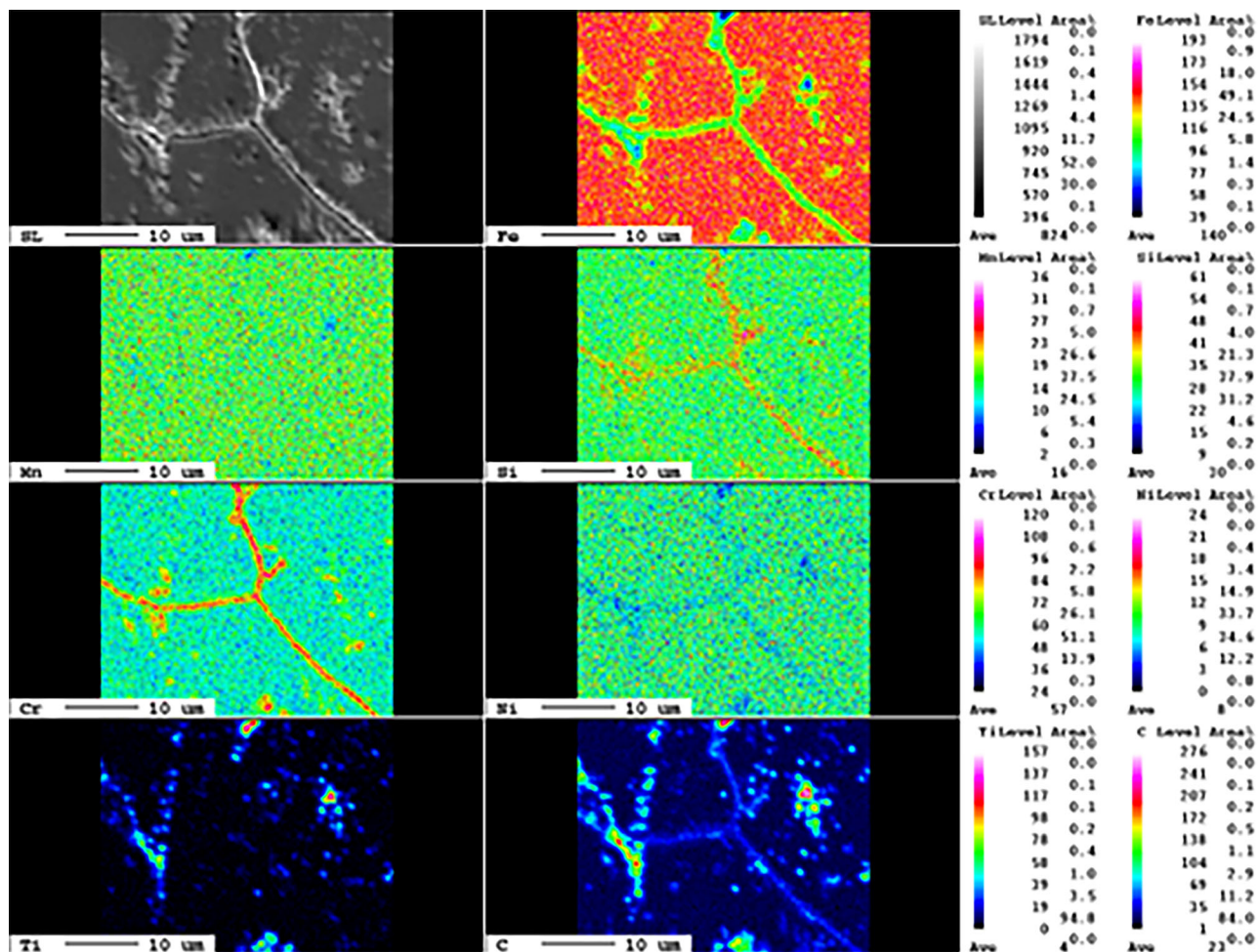


Fig. 4. EPMA element mapping of 10Mn7Cr0.5Ti alloy aged at 800°C.

precipitated at the grain boundaries, and  $\text{Cr}_{23}\text{C}_6$  and  $\text{Cr}_7\text{C}_3$  are formed at higher temperatures. The NbC does not dissolve at higher aging temperatures and has a strong influence on the shape memory effect.

The XRD patterns of Fe-10Mn-6Si-4Ni-7Cr-0.3C-mTi alloys aged at 800°C are presented in Fig. 7. The main peaks are indicated at 42–45°. It can be visualized that the  $\text{Cr}_7\text{C}_3$  (421) and  $\text{Cr}_7\text{C}_3$  (112) peaks are consistent.<sup>26</sup> Small peak intensities of  $\text{Cr}_{23}\text{C}_6$  (422) and  $\alpha'$  martensite are also present at higher temperatures. The formation of  $\alpha'$  martensite depletes the shape memory effect of the alloy. Both Cr carbides ( $\text{Cr}_{23}\text{C}_6$  and  $\text{Cr}_7\text{C}_3$ ) are present in the alloy when aged at 800°C. There is also a weak signal peak between 35° and 38°, which is found to be TiC (111). The formation of TiC and Cr carbides under high-temperature aging improves the shape memory effect.<sup>27</sup>

Figure 8 presents the XRD analysis of Fe-10Mn-6Si-4Ni-7Cr-0.3C-nNb alloys at different temperatures. It can be seen that there are two obvious signal peaks between 41° and 43° and 44–45°. The signal peaks present at 45–49°, are consistent with

$\text{Cr}_{23}\text{C}_6$  (422) and  $\text{Cr}_{23}\text{C}_6$  (511). It can also be seen that the  $\text{Cr}_7\text{C}_3$  (112) signal is significantly weakened at 800°C, indicating that the  $\text{Cr}_7\text{C}_3$  in the alloy is also relatively reduced. The reduction of  $\text{Cr}_7\text{C}_3$  will reduce the shape memory effect, while the precipitation of NbC can improve the shape memory effect. The NbC peaks are significantly increased at 900°C. If the volume fraction of NbC in the alloy is less than 15%, the signal will not be easily generated. Therefore, when the amount of added Nb is reduced, the NbC signal will be undetectable.<sup>22</sup>

It has been observed from the XRD and SEM analyses that  $\text{Cr}_7\text{C}_3$  and  $\text{Cr}_{23}\text{C}_6$  phases are formed at high-temperature aging. The 10Mn7Cr with 0.5 Ti alloy indicated the best shape memory effect and was selected for TEM observations. The formation temperature of TiC was 900°C.

In order to further analyze the morphology and distribution of TiC in the alloy, a TEM brightfield image of the 10Mn7Cr0.5Ti alloy aged at 900°C is presented in Fig. 9, from which it can be seen that the morphology of TiC is irregular and granular, as described in the SEM images (Fig. 3). The XRD analysis indicated that the TiC crystal structure is a

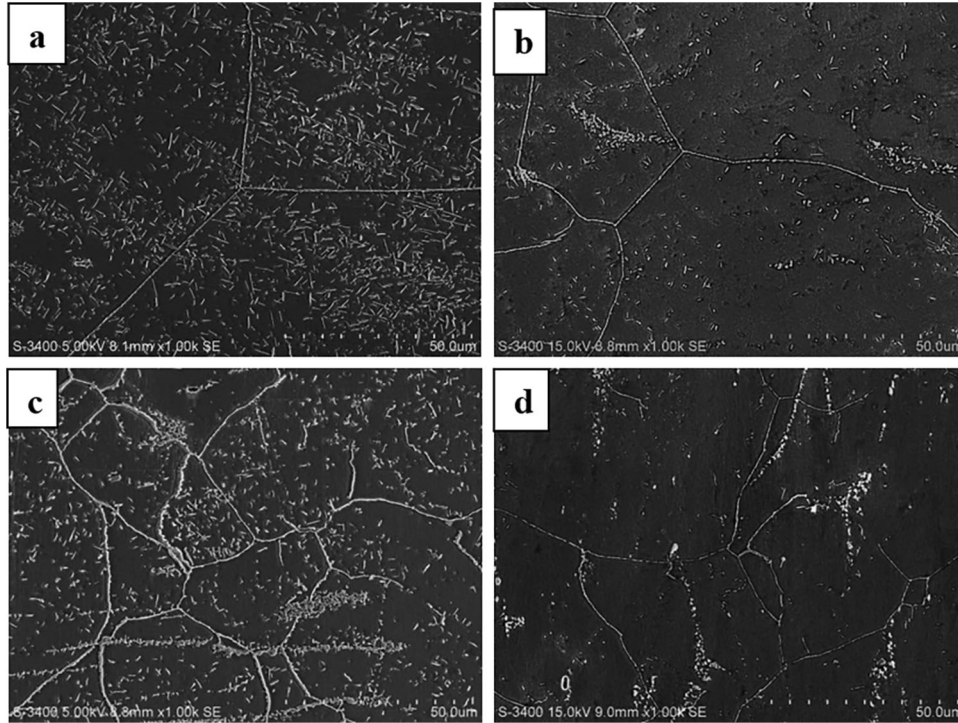


Fig. 5. SEM images of: (a) 10Mn7Cr 0.05Nb, (b) 10Mn7Cr 0.1Nb, (c) 10Mn7Cr 0.3Nb, and (d) 10Mn7Cr 0.5Nb alloys after aging 800°C.

common cubic FCC structure with a lattice constant of 0.43 nm. TEM observations confirmed that it has an FCC structure with a lattice constant of 0.44 nm, indicating that the second precipitated phase is TiC, and also proving that it exists after high-temperature (900°C) aging.<sup>21,28</sup> The slight error in the lattice constant may be caused by: (1) because the JCPD card data is a standard carbide of Ti and C, and that the alloy in this study is added with Fe, Cr, Ti, and other metal elements, and (2) SAPD is obtained by manually importing the analysis program, and there may be some errors in the interpretation.<sup>29</sup>

### Shape Memory Effect

The shape recovery ratios (RSME) of Fe-10Mn-6Si-4Ni-7Cr-0.3C-mTi alloys measured at 3% bending strain is presented in Fig. 10 and summarized in Table I, from which it can be seen that the RSMEs of all the alloys increase with the increase in aging temperature, reaching the maximum at 800°C. The best RSME for Fe-10Mn-6Si-4Ni-7Cr-0.3C alloys with 0 Ti, 0.1 Ti, 0.3 Ti, 0.5 Ti, and 0.7 Ti were 85.0%, 89.9%, 89.5%, 91.1%, and 74.4% at 800°C respectively. The increase in Ti contents improves the RSME of the alloy and reaches the maximum (91.1%) with 0.5 Ti addition. The further addition of Ti will decrease the RSME. The 10Mn7Cr0.5Ti alloy after aging at 800°C gave the best RSME of 91.1%. The 0.5 Ti addition has increased by 6.1 % RSME when compared with the Fe-10Mn-6Si-4Ni-7Cr-

0.3C alloy. A large amount of Cr carbides ( $\text{Cr}_{23}\text{C}_6$ ,  $\text{Cr}_7\text{C}_3$ ) are generated inside the alloy when aged at high temperature ( $\geq 800^\circ\text{C}$ ). These carbides effectively separate the parent phase, readily forming a single variant of  $\varepsilon$  martensite, which subsequently facilitates a high ratio of shape recovery.<sup>30,31</sup> The Ti addition also improves the shape memory effect at lower aging temperatures. The 0.5 Ti has improved the RSME by 20–30% at 500°C and 600°C aging temperatures. The recovery ratio can also be increased by 10–20% when aged at 700°C.<sup>8,25,32</sup>

It is also indicated from the XRD analysis (Fig. 7) that the alloy aged at 800°C has a higher proportion of  $\text{Cr}_7\text{C}_3$ , while the alloy aged at 900°C has a higher proportion of  $\text{Cr}_{23}\text{C}_6$ . The higher proportion of  $\text{Cr}_7\text{C}_3$  has a better shape memory effect.<sup>1,17</sup> TiC phase formation makes  $\alpha'$  martensite less likely to be generated and effectively improves the RSME.<sup>1</sup> It can be seen that TiC mostly contributes the increase in RSME after aging at lower temperatures, but the improved RSME is limited.<sup>33</sup>

The shape recovery rate of the 10Mn7Cr alloy with different compositions of Nb are presented in Fig. 11 and summarized in Table I. The best RSME (88.6%) was observed in the 10Mn7Cr alloy with 0.005 Nb at 900°C, which is 3.6% higher than the 10Mn7Cr alloy.<sup>6,34</sup> It can also be observed from Fig. 11 that the RSME of the 10Mn7Cr alloy is increased with the addition of the small amount of Nb, but the recovery ratio will obviously decrease when the addition amount is greater than 0.1 wt.%

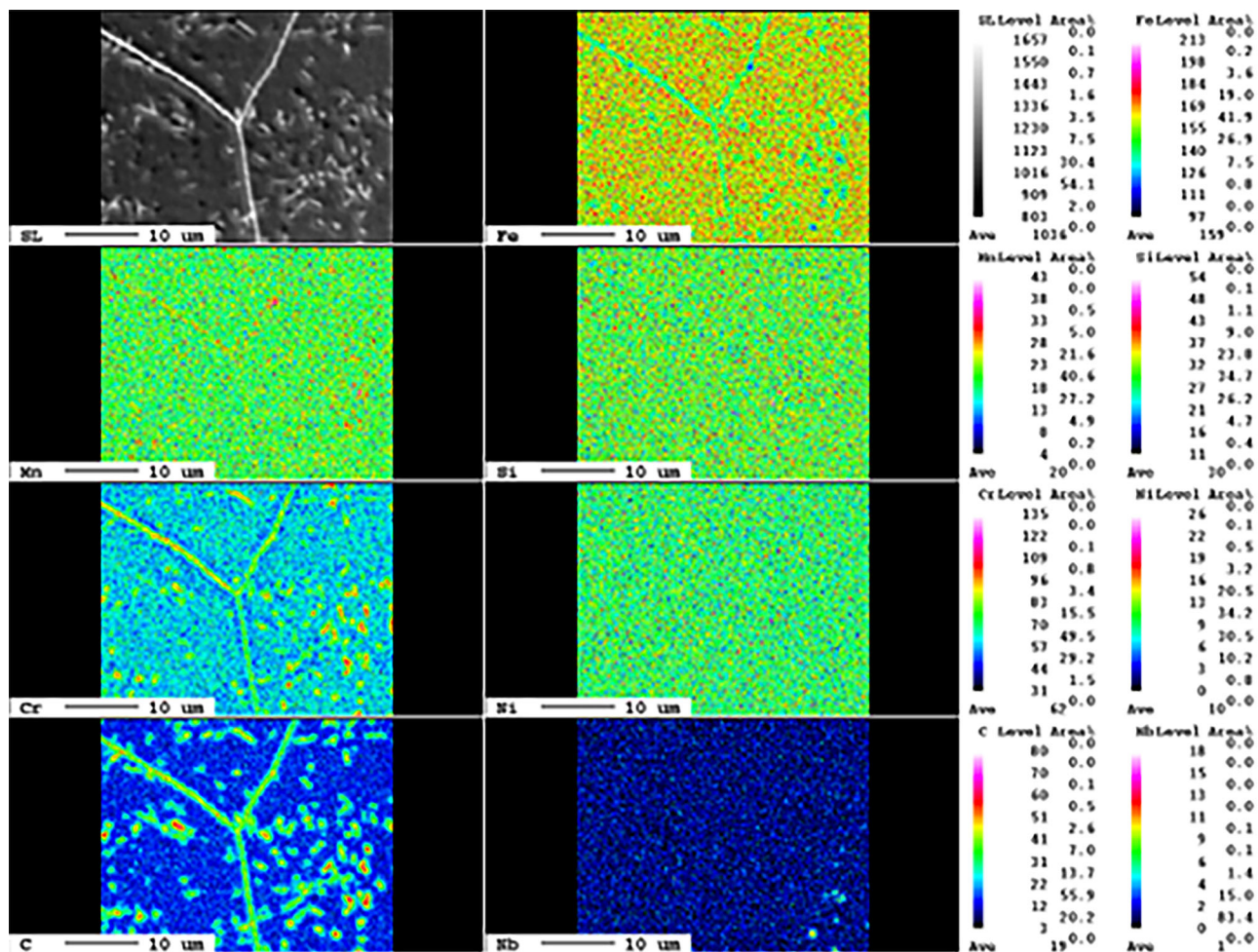


Fig. 6. EPMA element mapping of 10Mn7Cr0.05Nb alloy aged at aged at 800°C.

Nb.<sup>35,36</sup> The RSME of the alloys is increased at lower aging temperatures of 500–700°C by about 5–30%, indicating that the addition of Nb at lower aging temperatures can still improve the RSME.<sup>37,38</sup> The formation of NbC at lower aging temperatures makes  $\alpha'$  martensite generation difficult and increases the RSME. The enhancement in the RSME of the alloys is contributed to by NbC.<sup>39,40</sup>

It can be seen from Table I that each alloy has the best RSME at 800°C or 900°C. The formation of NbC and the precipitation of  $\text{Cr}_{23}\text{C}_6$  and  $\text{Cr}_7\text{C}_3$  is the main reason for improving the RSME.<sup>18</sup> The precipitation of Cr is also significantly reduced after aging at 800°C with the addition of 0.3 Nb and 0.5 Nb alloys.<sup>41</sup> The addition of too much Nb and aging at high temperatures will inhibit the formation of Cr carbides ( $\text{Cr}_{23}\text{C}_6$  and  $\text{Cr}_7\text{C}_3$ ), resulting in a decrease in the shape memory effect.<sup>19</sup>

### Chemical Corrosion Analysis

The samples with the conditions presenting the maximum RSME were selected for corrosion analysis. Only three samples with the composition of

10Mn7Cr, 10Mn7Cr0.5Ti, and 10Mn7Cr0.05Nb were selected for the chemical corrosion analysis. The Tafel curves are presented in Fig. 12 and the electrochemical properties are summarized in Table II. Higher corrosion resistance is represented by a higher corrosion potential and lower current density. The addition of 0.5 Ti in 10Mn7Cr followed by aging at 800°C has improved the RSME from 85% to 91.1%, and the corrosion potential is enhanced from  $-1.521$  V to  $-1.242$  V.<sup>42</sup> This indicates that Ti is an efficient additive and that 800°C is the effective aging temperature to improve the RSME and the corrosion resistance. The presence of Cr contents improves the corrosion resistance more effectively. Smooth Tafel curves have been observed (Fig. 12) which indicates the absence of pitting.<sup>43–45</sup> The 0.5 Ti addition in the 10Mn7Cr alloys followed by aging at 800°C leads to the formation and coexistence of  $\text{Cr}_7\text{C}_3$  rod-like elongated  $\text{Cr}_7\text{C}_3$  and irregular granular-shaped TiC (Figs. 3, 4). These carbides lead to an enhancement in corrosion resistance. Another reason for the corrosion resistance improvement is the formation of noble and passive

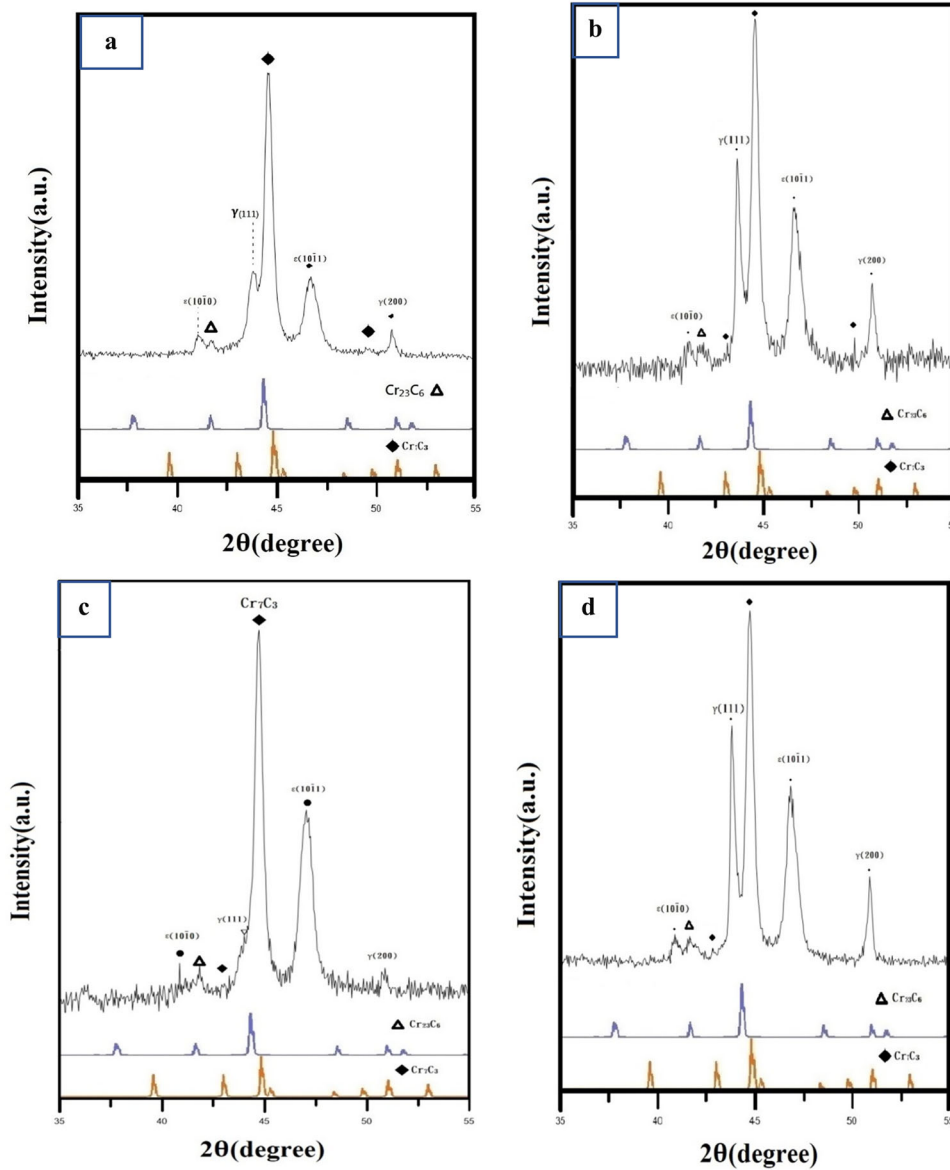


Fig. 7. XRD patterns of: (a) 10Mn7Cr 0.1Ti, (b) 10Mn7Cr 0.3Ti, (c) 0.5Ti, and (d) 10Mn7Cr0.7Ti alloys after aging at 800°C.

titanium oxide film on the surface. The presence of compact and stable film is the potential reason against pitting corrosion.

The addition of the slight amount of Nb in 10Mn7Cr and aging at 900°C is more efficient than Ti in corrosion resistance improvement. The corrosion potential of 10Mn7Cr0.05Nb samples after aging at 900°C increased to  $-1.446$  V, indicating the highest corrosion resistance among the alloyed samples.<sup>46</sup> The addition of Nb leads to the formation of  $\text{Cr}_{23}\text{C}_6$ ,  $\text{Cr}_7\text{C}_3$ , and NbC within the grain boundaries (Figs. 5, 6). The maximum carbides are present in 10Mn7Cr0.05Nb which causes the improvement in corrosion resistance. The further addition of Nb causes a decrease in carbide

precipitates and consequently decreases the corrosion resistance. NbC is also formed during the hot-rolling process and causes the precipitation-hardening of the carbide phases. The higher Nb contents have a negative impact on the RSME at all aging conditions; thus, they have not been selected for corrosion analysis. Similar Tafel curves in all the samples indicate that a similar corrosion mechanism occurred in all the alloys.<sup>42</sup> The higher corrosion resistance in 10Mn7Cr0.05Nb can also be attributed to the improved homogeneity of austenite due to the long aging time. The  $\beta$ -Mn-phase has been dissolved and the  $\gamma$ -phase developed at a higher aging temperature, which eventually act as cathodes in galvanic corrosion to improve the



Effects of Ti and Nb Additions on Microstructure and Shape Memory  
 Effect of Fe-10Mn-6Si-4Ni-7Cr-0.3C Shape Memory Alloy

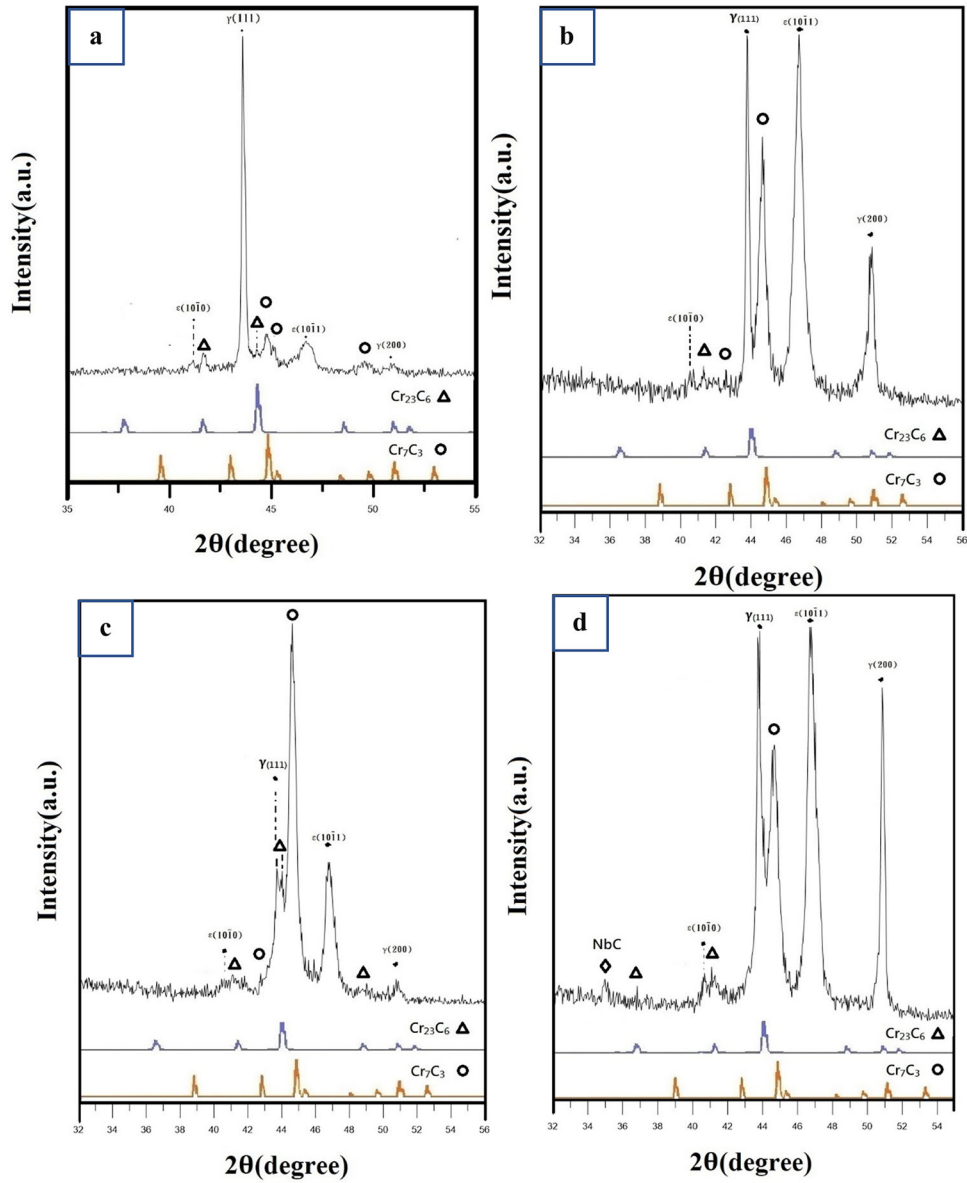


Fig. 8. XRD patterns of: (a) 10Mn7Cr0.05Nb, (b) 10Mn7Cr 0.1Nb, (c) 10Mn7Cr0.3Nb, and (d) 10Mn7Cr 0.5Nb alloys after aging at  $900^{\circ}\text{C}$ .

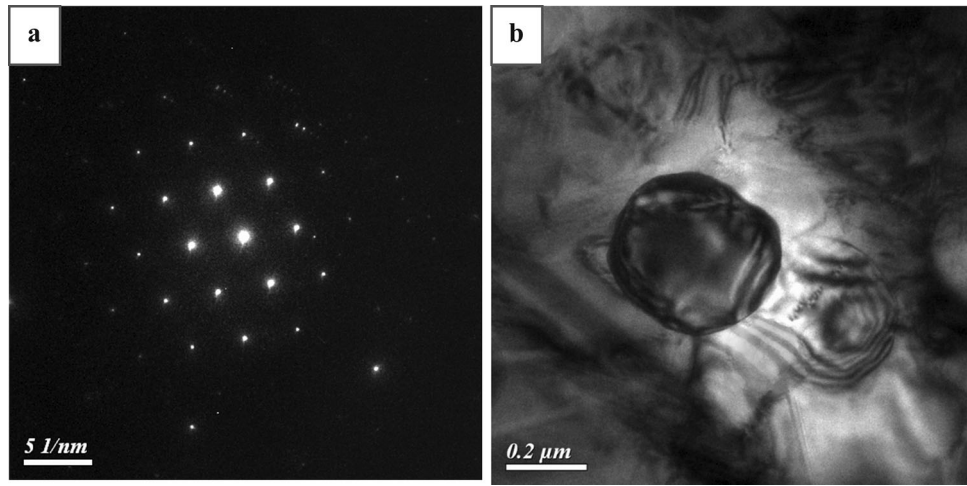


Fig. 9. (a) TEM brightfield image of 10Mn7Cr0.5Ti alloy, (b) SADP diagram of 10Mn7Cr0.5Ti aged at  $900^{\circ}\text{C}$ .

corrosion resistance. The  $\gamma$ -phase appears to be more noble to restrict the corrosion damage.

The Ti is a better electrical conductor compared to Nb and has a smaller energy barrier to start the chemical reaction of corrosion. It has more cathodes and anodes on the surface which leads to higher corrosion relative to Nb-reinforced alloys.

## CONCLUSION

VAR melting has been employed to process low-manganese iron-based SMAs for experimental investigations. The incorporation of titanium (Ti) and niobium (Nb), coupled with the application of suitable ageing treatments, has led to the achievement of noteworthy shape memory effects. The significant experimental outcomes are outlined below.

1. The addition of small amounts of Ti and Nb in the 10Mn7Cr alloy and aging at 800°C produced a large amount of second-phase precipitates ( $\text{TiC}$ ,  $\text{NbC}$ ,  $\text{Cr}_{23}\text{C}_6$ , and  $\text{Cr}_7\text{C}_3$ ) which

can improve the shape memory effect of the alloy.

2. The best RSME for 10Mn7Cr0.5Ti and 10Mn7Cr0.005Nb was found to be 91.1% and 88.6% at 800°C and 900°C, respectively.
3. The increase in Ti concentration and aging at higher temperatures gradually increased the shape memory effect. The 0.5 Ti addition improved the RSME by 6.1%, and 0.7 Ti will decrease the RSME.
4. The Ti addition at lower aging temperatures also enhanced the shape memory effect. The RSME of alloys with Ti additions at 500–600°C aging temperature increased by 20–30% and at 700°C by about 10–20%.
5. The highest corrosion resistance was observed for the 10Mn7Cr0.5Ti and 10Mn7Cr0.05Nb alloys for their higher corrosion potentials of  $-1.242$  V and  $-1.446$  V, respectively.
6. It is evident that VAR melting is not a viable option for industrial-scale mass production. Consequently, the utilization of industrial-

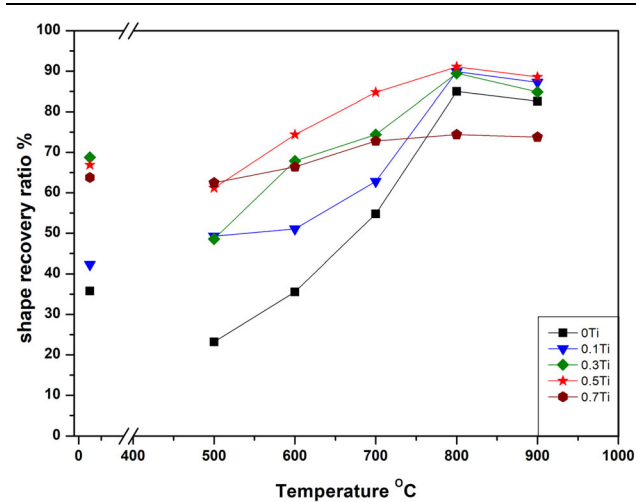


Fig. 10. Shape recovery ratio of 10Mn7Cr alloy with mTi contents.

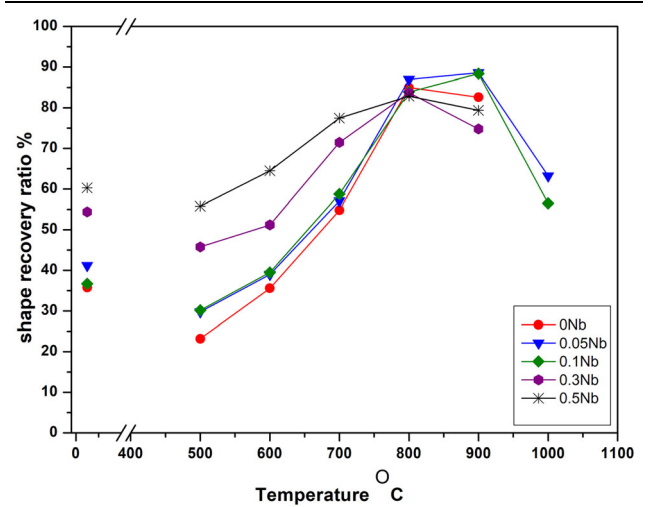


Fig. 11. Shape recovery ratio of 10Mn7Cr alloy with nNb contents.

**Table I. Shape recovery ratio of 10Mn7Cr alloy with mTi/xNb at different temperatures**

Alloy	Solution treatment	500°C	600°C	700°C	800°C	900°C
10Mn7Cr 0Ti	35.8	23.2	35.6	54.8	85.0	82.6
10Mn7Cr0.1Ti	42.3	49.3	51.1	62.8	89.9	87.2
10Mn7Cr0.3Ti	68.8	48.6	67.9	74.4	89.5	84.9
10Mn7Cr0.5Ti	66.9	61.2	74.4	84.8	91.1	88.6
10Mn7Cr0.7Ti	63.8	62.5	66.4	72.8	74.4	73.8
10Mn7Cr 0Nb	35.8	23.2	35.6	54.8	85.0	82.6
10Mn7Cr0.05Nb	41.2	29.8	39.0	57.1	87.0	88.6
10Mn7Cr0.1Nb	36.7	30.2	28.0	54.9	79.5	88.4
10Mn7Cr0.3Nb	54.4	45.8	51.2	71.5	83.7	74.8
10Mn7Cr0.5Nb	60.3	55.8	64.5	77.5	82.9	79.4

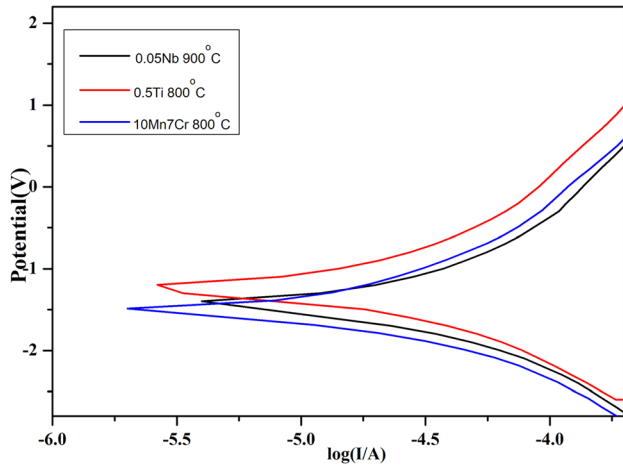


Fig. 12. Tafel curves of 10Mn7Cr-mTi/nNb alloys in 3.5-wt.% NaCl solution.

**Table II. Electrochemical corrosion properties of mTi/xNb alloys with best performance**

	$E_{\text{corr}}$ (V)	$I_{\text{corr}}$ (A)
10Mn7Cr-800°C	- 1.521	$1.238 \times 10^{-5}$
0.5Ti-800°C	- 1.242	$1.412 \times 10^{-5}$
0.05Nb-900°C	- 1.446	$2.403 \times 10^{-5}$

scale mass-production equipment is recommended for the melting of high-quality low-manganese Fe-based SMAs, with the objective of facilitating their actual industrial applications.

### ACKNOWLEDGEMENTS

The authors are pleased to acknowledge the financial support of this research by the Ministry of Science and Technology (National Science Council), Republic of China, under Grant No. MOST 109-3116-F-002-004-CC1.

### CONFLICT OF INTEREST

The authors declare that they have no known competing financial interests or personal relationships that could have appeared to influence the work reported in this paper.

### REFERENCES

1. L.M. Guerrero, P. La Roca, F. Malamud, A. Baruj, and M. Sade, *Shape Mem. Superelast.* 6, 202 <https://doi.org/10.1007/s40830-020-00285-z> (2020).
2. M.Y. Hasbi, E. Mabururi, S.D. Yudanto, F.M. Ridlo, B. Adjiantoro, D. Irawan, I.G.P. Astawa, M.R. Rido, T.B. Romijarso, R. Roberto, D.P. Utama, and N. Amalia, Opportunities and challenges of Fe-based shape memory alloys for

- biomedical applications—Short review (2024). p. 020054. <https://doi.org/10.1063/5.0186259>.
3. F. Baghdadi, A. Uzumcu, and I. Mutlu, *Braz. J. Phys.* 52, 175 <https://doi.org/10.1007/s13538-022-01179-4> (2022).
4. Z. Liu, Z. Dong, L. Hu, H. Zhu, G. Wu, Y. Wen, and X.-L. Zhao, *Structures* 61, 106049 <https://doi.org/10.1016/j.istruc.2024.106049> (2024).
5. E. Farber, J.-N. Zhu, A. Popovich, and V. Popovich, *Mater. Today Proc.* <https://doi.org/10.1016/j.matpr.2020.01.563> (2020).
6. A.-M. Roman, R. Cimpoeșu, B. Pricop, M.M. Cazacu, G. Zegan, B. Istrate, A. Cocean, R. Chelariu, M. Moscu, G. Bădărău, N. Cimpoeșu, and M.C. Ivănescu, *Nanomaterials* 14, 330 <https://doi.org/10.3390/nano14040330> (2024).
7. T. Kikuchi and S. Kajiwara, *Shape Memory Effect in an Unaugmented Fe-Ni-Co-Ti Alloy*. *Ecomaterials* (Elsevier, Amsterdam, 1994), pp989–992. <https://doi.org/10.1016/B978-1-4832-8381-4.50231-6>.
8. A.-M. Roman, I. Voiculescu, R. Cimpoeșu, B. Istrate, R. Chelariu, N. Cimpoeșu, G. Zegan, C. Panaghie, N.M. Lohan, M. Axinte, and A.M. Murariu, *Crystals (Basel)* 13, 109 <https://doi.org/10.3390/cryst13010109> (2023).
9. M. Vollmer, A. Bauer, M.J. Kriegel, M. Motylenko, and T. Niendorf, *Scripta Mater.* 194, 113619 <https://doi.org/10.1016/j.scriptamat.2020.10.057> (2021).
10. B. Kustov, E. Lähderanta, J. Van Humbeeck, and S.J. Torrens, *J. Market. Res.* 30, 6641 <https://doi.org/10.1016/j.jmrt.2024.05.076> (2024).
11. H. Khodaverdi, M. Mohri, A.S. Ghorabaei, E. Ghafoori, and M. Nili-Ahmadabadi, *Mater Charact* 195, 112486 <https://doi.org/10.1016/j.matchar.2022.112486> (2023).
12. A. Walsch, M.J. Kriegel, M. Motylenko, G. Korpala, U. Prael, and A. Leineweber, *Scripta Mater.* 192, 26 <https://doi.org/10.1016/j.scriptamat.2020.10.003> (2021).
13. Y. Yang, C. Leinenbach, and M. Shahverdi, *J. Alloys Compd.* 940, 168856 <https://doi.org/10.1016/j.jallcom.2023.168856> (2023).
14. Q. Zhang, P. Xu, T. Jiang, S. Li, C. Yu, and D. Yang, *Optik (Stuttg)* 271, 170202 <https://doi.org/10.1016/j.ijleo.2022.170202> (2022).
15. P.S. Nnamchi, A. Younes, O.A. Fasuba, C.S. Obayi, and P.O. Offor, *Tribol. Mater. Surf. Interfaces* 16, 317 <https://doi.org/10.1080/17515831.2022.2086780> (2022).
16. M. Koster, W.J. Lee, M. Schwarzenberger, and C. Leinenbach, *Mater. Sci. Eng. A* 637, 29 <https://doi.org/10.1016/j.msea.2015.04.028> (2015).
17. Y. Shen, W. Sun, Z. Wei, J. Li, J. Guo, K. Wang, et al., *J. Alloys Compd.* 832, 154830 <https://doi.org/10.1016/j.jallcom.2020.154830> (2020).
18. L. Yong, Q. Luo, H. Peng, J. Yan, B. Xu, and Y. Wen, *Mater Charact* 169, 110650 <https://doi.org/10.1016/j.matchar.2020.110650> (2020).
19. D. Kim, I. Ferretto, C. Leinenbach, W. Lee, and W. Kim, *Mater Charact* 197, 112705 <https://doi.org/10.1016/j.matchar.2023.112705> (2023).
20. M. Mohri, I. Ferretto, H. Khodaverdi, C. Leinenbach, and E. Ghafoori, *J. Market. Res.* 24, 5922 <https://doi.org/10.1016/j.jmrt.2023.04.195> (2023).
21. K. Hirata, X. Xu, T. Omori, and R. Kainuma, *J. Magn. Mater.* 500, 166311 <https://doi.org/10.1016/j.jmmm.2020.166311> (2020).
22. Y. Wang, X. Deng, M. Zhang, and H. Yang, *Mater Res Express* 9, 126511 <https://doi.org/10.1088/2053-1591/acabb4> (2022).
23. F. Malamud, L.M. Guerrero, P. La Roca, M. Sade, and A. Baruj, *Mater. Des.* 139, 314 <https://doi.org/10.1016/j.matdes.2017.11.017> (2018).
24. X.-L. Gu, Z.-Y. Chen, Q.-Q. Yu, and E. Ghafoori, *Eng. Struct.* 243, 112710 <https://doi.org/10.1016/j.engstruct.2021.112710> (2021).
25. H.B. Peng, J.B. Zhang, L.X. Sun, F. Song, X.G. An, H. Wang, and Y.H. Wen, *Mater. Sci. Eng. A* 852, 143675 <https://doi.org/10.1016/j.msea.2022.143675> (2022).

26. D. Kim, E. Choi, H. Cheon, and W. Kim, *J. Mater. Eng. Perform.* <https://doi.org/10.1007/s11665-023-08587-w> (2023).
27. Q. Zou, X. Ye, Y. Li, W. Luo, X. Yang, and Y. Luo, *Mater. Chem. Phys.* 293, 126992 <https://doi.org/10.1016/j.matchemphys.2022.126992> (2023).
28. T. Saito, C.Z. Kapusta, and A. Takasaki, *Mater. Sci. Eng. A* 592, 88 <https://doi.org/10.1016/j.msea.2013.10.097> (2014).
29. M. Mohri, I. Ferretto, C. Leinenbach, D. Kim, D.G. Lignos, and E. Ghafoori, *Mater. Sci. Eng. A* 855, 143917 <https://doi.org/10.1016/j.msea.2022.143917> (2022).
30. X.H. Min, T. Sawaguchi, K. Ogawa, T. Maruyama, F.X. Yin, and K. Tsuzaki, *J. Alloys Compd.* 577, S478 <https://doi.org/10.1016/j.jallcom.2012.02.140> (2013).
31. E. Fritsch, M. Izadi, and E. Ghafoori, *Constr. Build. Mater.* 229, 117042 <https://doi.org/10.1016/j.conbuildmat.2019.117042> (2019).
32. Q. Zou, X. Ye, Y. Li, W. Luo, and Y. Luo, *J. Mater. Sci.* 58, 3346 <https://doi.org/10.1007/s10853-023-08239-3> (2023).
33. D. Kim, E. Choi, H. Cheon, and W. Kim, *J. Mater. Eng. Perform.* 33, 2253 <https://doi.org/10.1007/s11665-023-08587-w> (2024).
34. Y. Luo, Y. Fu, W. He, H. Peng, and Y. Wen, *Adv. Eng. Mater.* <https://doi.org/10.1002/adem.202400475> (2024).
35. W. Li, S. Zuo, M. Khedr, X. Li, K. Xiong, and F. Xiao, *J. Market. Res.* 30, 5394 <https://doi.org/10.1016/j.jmrt.2024.04.261> (2024).
36. A. Tabrizikahou, J. Białasik, S. Borysiak, M. Fabisiak, M. Łasecka-Plura, T. Jesionowski, and M. Kuczma, *Arch. Civ. Mech. Eng.* 24, 189 <https://doi.org/10.1007/s43452-024-01004-6> (2024).
37. J.G. Lopes, D. Martins, K. Zhang, B. Li, B. Wang, X. Wang, N. Schell, E. Ghafoori, A.C. Baptista, and J.P. Oliveira, *J. Mater. Sci.* 59, 7387 <https://doi.org/10.1007/s10853-024-09606-4> (2024).
38. M. Golrang, M. Mohri, E. Ghafoori, H. Khodaverdi, and M. Nili-Ahmadabadi, *J. Market. Res.* 29, 1887 <https://doi.org/10.1016/j.jmrt.2024.01.248> (2024).
39. M. Mandel, V. Kietov, R. Hornig, M. Vollmer, J.-M. Frenck, C. Wüstefeld, D. Rafaja, T. Niendorf, and L. Krüger, *Corros. Sci.* 179, 109172 <https://doi.org/10.1016/j.corsci.2020.109172> (2021).
40. H. Hong, B. Gencturk, and M.S. Saiidi, *Smart Mater. Struct.* 33, 075001 <https://doi.org/10.1088/1361-665X/ad4d5f> (2024).
41. X. Ma, X. Ding, R. Chen, X. Chen, Q. Song, and H. Cui, *Intermetallics (Barking)* 157, 107885 <https://doi.org/10.1016/j.intermet.2023.107885> (2023).
42. H. Liu, Y. Yan, X. Wu, H. Fang, X. Chu, J. Huang, et al., *J. Alloys Compd.* 859, 157755 <https://doi.org/10.1016/j.jallcom.2020.157755> (2021).
43. X. Liu, P. Xu, L. Yao, X. Li, C. Pang, L. Yang, and Y. Liang, *J. Mech. Sci. Technol.* 36, 5027 <https://doi.org/10.1007/s12206-022-0915-y> (2022).
44. M.K. El Fawkhry, *J. Market. Res.* 15, 1069 <https://doi.org/10.1016/j.jmrt.2021.08.009> (2021).
45. M.-M. Pan, X.-M. Zhang, D. Zhou, R.D.K. Misra, and P. Chen, *Mater. Sci. Eng. A* 797, 140107 <https://doi.org/10.1016/j.msea.2020.140107> (2020).
46. D. Dias, S. Nakamatsu, C.A. Della Rovere, J. Otubo, and N.A. Mariano, *Metals (Basel)* 10, 13 <https://doi.org/10.3390/met10010013> (2019).

**Publisher's Note** Springer Nature remains neutral with regard to jurisdictional claims in published maps and institutional affiliations.

Springer Nature or its licensor (e.g. a society or other partner) holds exclusive rights to this article under a publishing agreement with the author(s) or other rightsholder(s); author self-archiving of the accepted manuscript version of this article is solely governed by the terms of such publishing agreement and applicable law.